Journal of Solid State Electrochemistry
https://doi.org/10.1007/s10008-020-04866-x

ORIGINAL PAPER

Electrochemical performance of magnetic nanoparticle-decorated reduced graphene oxide (MRGO) in various aqueous electrolyte solutions

S. M. Patil[1] · S. R. Shingte[1] · V. C. Karade[2] · J. H. Kim[2] · R. M. Kulkarni[3] · A. D. Chougale[4] · P. B. Patil[1]

Received: 25 May 2020 / Revised: 7 November 2020 / Accepted: 9 November 2020

Abstract

The objective of this work is twofold: (1) to improve the electrochemical performance of reduced graphene oxide (RGO) by decorating RGO sheets with magnetic nanoparticles (MNPs) and (2) to evaluate the electrochemical performance of RGO and MNP-decorated RGO (MRGO) in various aqueous electrolyte solutions (phosphate buffer solution (PBS) containing ferricyanide, PBS containing ferricyanide and KCl, Na_2SO_4, and KOH). The morphological and structural characteristics of solvothermal synthesized RGO and MRGO revealed the decoration of phase pure Fe_3O_4 nanoparticles on RGO sheets. In FC-PBS-KCl electrolyte solution, MRGO showed higher redox peak current (83.89 μA) and lower peak potential separation (0.11 V) at 50 mV s^{-1} scan rate compared with that in FC-PBS electrolyte solution. MRGO showed 15.5% higher peak current than that for the RGO in FC-PBS-KCl electrolyte solution. Moreover, the peak current for MRGO in FC-PBS-KCl was increased by 30% when compared with that in FC-PBS electrolyte solution. These results suggest that MRGO in FC-PBS-KCl electrolyte solution can be a good electron pathway between electrode and electrolyte solution for sensing applications. On the other hand, in both Na_2SO_4 and KOH electrolyte solution, RGO and MRGO showed supercapacitive behavior. In KOH, MRGO exhibited higher specific capacitance (180 Fg^{-1} at 3 A g^{-1}) and superior cyclic stability (87% after 2000 cycles) compared with that in Na_2SO_4. MRGO showed 219% increase in specific capacitance than that of the RGO in KOH electrolyte solution. The superior electrochemical performance of MRGO compared with that of RGO is attributed to the synergistic effect of conductivity of RGO and redox activity of MNPs.

Keywords Reduced graphene oxide · Magnetic reduced graphene oxide · Electrolyte solutions · Electrochemical performance · Electrochemical sensing · Supercapacitor

Introduction

Recently, carbon and carbon-based nanostructures like graphene, carbon nanotubes (CNTs) [1], fullerene (C_{60}) [2], and reduced graphene oxide (RGO) [3] have become the center of interest due to their astonishing physiochemical properties. Carbon and its allotropes like RGO, CNTs, and nanofibers (NFs) are ideal materials for electrochemical biosensing platforms [4], and for high power and energy storage applications [5]. Carbon can hybridize into sp, sp^2, and sp^3 configurations with small gaps between their 2s and 2p electron shells, which is useful for the sensing of biological and pharmaceutical analytes [6]. Carbon-based materials show a significant advantage in supercapacitor applications due to their extraordinary properties, such as high surface area, porosity, and morphology [7]. The graphene oxide (GO) is a 2D carbon sheet with a honeycomb-like structure comprising a mixture of sp^2 and sp^3-hybridized carbon atoms that have been attracting and gaining more attention. GO can be economically and effortlessly produced on a large scale from graphite [8]. The resulting GO from exfoliation of graphite oxide has

✉ P. B. Patil
prashantphy@gmail.com

[1] Department of Physics, The New College, Shivaji University, Kolhapur, Maharashtra 416012, India

[2] Optoelectronic Convergence Research Center and Department of Materials Science and Engineering, Chonnam National University, Gwangju 500-757, South Korea

[3] School of Nanoscience and Technology, Shivaji University, Kolhapur, Maharashtra 416004, India

[4] Department of Chemistry, The New College, Shivaji University, Kolhapur, Maharashtra 416012, India

Published online: 18 November 2020

abundant functional groups on the GO surface, such as a –COOH (Carboxyl), epoxy, and –OH (hydroxyl), making it useful for diverse applications [9]. RGO is indeed a form of graphene with similar properties. RGO produced directly from graphite exhibits the superior electrochemical response owing to residual oxygen functional groups and defects [10, 11]. RGO can be synthesized by numerous methods like chemical reduction [12], thermal reduction [13], microwave-assisted [14], photocatalytic reduction [10], and solvothermal/hydrothermal method [15].

In comparison with carbaneous materials, metal oxide has shorter cyclic lives due to volume changes arising from the redox reaction. However, the incorporation of metal oxide with carbaneous material improves the degree of reversibility and cyclic stability [16, 17]. Recently, extensive research is being carried out for the development of RGO/metal oxide nanocomposites for improving electrochemical performance [18, 19]. RGO sheets provide a highly conductive matrix and support anchoring of metal oxide nanoparticles. The RGO has been synthesized in various composite forms using polymers [19], ceramics [20], metal oxides [21], and sulfides [22], etc. RGO/metal oxide composite displays enhancement in electrochemical properties due to the synergistic effect of the two components [23]. Various RGO/metal oxide nanocomposites have been prepared for different applications viz. RGO/Mn_2O_3 [21], RGO/MnO_2 [24], RGO/Co_3O_4 [25], and RGO/Fe_3O_4 [26]. Among the various metal oxide nanoparticles anchored on RGO, the magnetite (Fe_3O_4) composed of Fe^{2+} and Fe^{3+} valance ions is of more interest. Fe_3O_4 particles have a large operational potential window, low cost, and biocompatibility [27]. Fe_3O_4 nanoparticles with surface step atoms offer abundant electrochemical active sites [28]. However, MNPs exhibit limitations such as poor electrical conductivity and weak electrocatalytic activity [29, 30]. These issues with MNPs can be addressed by anchoring the MNPs on the RGO sheet.

Magnetic nanoparticle-decorated reduced graphene oxide (MRGO) is a promising candidate in the energy storage [30], electrochemical sensing [31], and metal ion removal applications [32] due to its superior electrochemical performance. MRGO has been synthesized by various methods such as coprecipitation method [33], the refluxing method [34], microwave thermal treatment [35], and solvothermal method [36]. Generally, GO can be reduced by a solvothermal route at low temperature and high pressure. The C/O ratio of RGO, synthesized by the solvothermal method, is higher than that produced by the chemical reduction at ambient pressure [37]. Thus, the solvothermal treatment more effectively removes the oxygen-containing functional groups. Zhu et al. have prepared α-Fe_2O_3/RGO for anode material in high-performance lithium-ion batteries by the microwave-assisted method [35]. Mustafa et al. have fabricated Fe_3O_4/RGO-starch nanocomposite by hydrothermal method with high capacitance [38]. Zhang et al. have fabricated Fe_2O_3/RGO composite for sodium-ion battery by solvothermal method, which has resulted in high stability and outstanding rate capability with high current [39]. Yang et al. have synthesized Fe_3O_4/RGO by solvothermal method for improving electrochemical performance in which they observed high current density up to 200 mA g^{-1} [40]. Peik-See et al. have prepared Fe_3O_4/RGO by solvothermal method for simultaneous electrochemical detection of dopamine and ascorbic acid [41]. Gao et al. have synthesized quasi-hexagonal Fe_2O_3 nanoplates/graphene composite using a solvothermal method for high-performance supercapacitor applications [42]. Based on these previous reports, it can be said that the hydrothermal method is a simple, inexpensive, and nontoxic method for synthesizing RGO and Fe_3O_4-RGO and useful for obtaining monodispersed uniformly distributed MNPs on RGO sheet.

In addition to the exposed surface area of the electrode, the electrochemical behavior of the electrode also depends on the electrolyte solutions. The nature of the electrolyte solutions can influence the interfacial charge transfer, structural stability, and the side reactions occurring on the surface of the electrode materials. The properties of an electrolyte solution such as ionic radius, molar conductivity, mobility of the ions, and Gibbs free energy have a significant influence on the size and migration speed of the solvated ions [43]. Therefore, the choice of appropriate electrolyte solution for electrode material is crucial. In the electrochemistry, organic and aqueous electrolyte solutions are extensively used. However, aqueous electrolyte solutions have advantages over organic electrolyte solutions such as high conductivity and unique mechanism of proton transport [44].

In this work, MRGO was prepared by a one-step solvothermal method where the reduction of GO and anchoring of MNPs on the RGO sheets simultaneously occurred. The electrochemical performance of modified RGO/GCE and MRGO/GCE electrodes in various electrolyte solutions (phosphate buffer solution (PBS) containing ferricyanide, PBS containing ferricyanide and KCl, Na_2SO_4, and KOH) was investigated. The results presented here provide valuable information about electrolyte solution suitable for RGO and MRGO electrode materials to explore it for sensing and supercapacitive applications.

Materials and methods

Materials

All the chemicals used were of analytical grade and used without further purification. Natural graphite flakes (NGF), sodium nitrate ($NaNO_3$), potassium permanganate ($KMnO_4$), hydrogen peroxide (H_2O_2), sulfuric acid (H_2SO_4), *N*-*N*-dimethyl formamide (DMF), potassium ferricyanide

($K_3[Fe(CN)_6]$), PBS, potassium chloride (KCl), potassium hydroxide (KOH), and sodium sulfate (Na_2SO_4) were procured from Sisco Research Laboratories (SRL), India. Iron(III) acetylacetonate ($Fe(acac)_3$) was procured from Sigma-Aldrich. De-ionized (DI) water was used throughout the experiment.

Synthesis of reduced graphene oxide and magnetic reduced graphene oxide

GO was synthesized using NGF via a modified Hummers' method. The prepared GO was washed several times with warm water by centrifugation to avoid precipitation of the slightly soluble salt of mellitic acid formed as a side reaction [37, 45]. To prepare RGO by the solvothermal method, GO powder was added in DMF (30 mL, 1 mg mL^{-1}) with continuous stirring, and the mixture was further stirred for 4 h. The reaction mixture was then transferred into a Teflon-lined stainless steel autoclave and heated at 200 °C for 20 h. After completion of the reaction, the autoclave was allowed to cool naturally. The obtained RGO was washed three times with ethanol and DI water and dried overnight in an oven at 60 °C. MRGO was prepared by a similar procedure, but instead of GO, $Fe(acac)_3$ and GO in 1:1 ratio in DMF (30 mL, 1 mg mL^{-1}) were used [45].

Preparation of modified electrodes

Glassy carbon electrode (GCE, 3 mm in diameter) was polished sequentially with 1.0-μm, 0.3-μm, and 0.05-μm-sized alumina powder until a mirror-shine surface was obtained. The GCE was sonicated in DI water after each stage of polishing. The 10 μL aliquot of RGO or MRGO dispersed in DMF (1 mg mL^{-1}) was dropped on the polished GCE. Modified electrodes were allowed to dry for 3 h at room temperature. Electrodes modified with RGO and MRGO nanocomposite were named as RGO/GCE and MRGO/GCE, respectively.

Characterizations

The crystallinity and phase of the samples were studied by X-ray diffractometer (XRD X'pert PRO, Philips, Netherlands) with Cu Kα radiation (λ = 1.54056 Å). Microstructure and particle size were investigated using a transmission electron microscope (TEM, Tecnai G2 S-Twin). To analyze the presence/absence of functional groups, infrared spectra were recorded in KBr pellets in the range 4000–400 cm^{-1} using a Fourier transform infrared spectrometer (FTIR, Jascospectrometer). The elemental and chemical states of samples were investigated by X-ray photoelectron spectroscopy (XPS, Thermo VG Scientific, UK) with a monochromatic Mg Kα (1253.6 eV) radiation source.

Electrochemical measurements

The electrochemical measurements such as cyclic voltammetry (CV), electrochemical impedance spectroscopy (EIS), and galvanostatic charge–discharge (GCD) were carried out using Metrohm Autolab PGSTAT204 electrochemical workstation. In a conventional three-electrode system, platinum spiral wire and Ag/AgCl electrodes were used as a counter electrode and reference electrode, respectively. Either unmodified GCE or modified RGO/GCE or MRGO/GCE were used as a working electrode. To investigate the electrochemical performance of modified electrodes, electrochemical measurements were carried out in various electrolyte solutions, viz. (i) 0.1 M PBS (pH 7.0) containing 2 mM $K_3Fe(CN)_6$ (FC-PBS), (ii) 0.1 M PBS (pH 7.0) containing 2 mM $K_3Fe(CN)_6$ and 0.1 M KCl (FC-PBS-KCl), (iii) 1 M Na_2SO_4, and (iv) 1 M KOH.

Results and discussion

Characterizations of RGO and MRGO

Figure 1 shows the XRD patterns of GO, RGO, and MRGO. In Fig. 1a, the peak at 10.1° corresponds to (001) orientation of GO. The peak observed at 42.1° is indicative of a turbostratic disorder due to incomplete oxidation [46]. In the XRD pattern of RGO shown in Fig. 1b, peak at 10.1° was disappeared while an intense peak around 24.1° corresponding to (002) planes of RGO was observed [47]. In the case of the MRGO pattern shown in Fig. 1c, along with (002) peak of RGO, several peaks corresponding to the cubic structure of Fe_3O_4 (JCPDS file no. 19-0629) were observed. The presence of characteristic peaks of RGO as well as peaks of Fe_3O_4 demonstrates the coexistence of MNPs and RGO in the

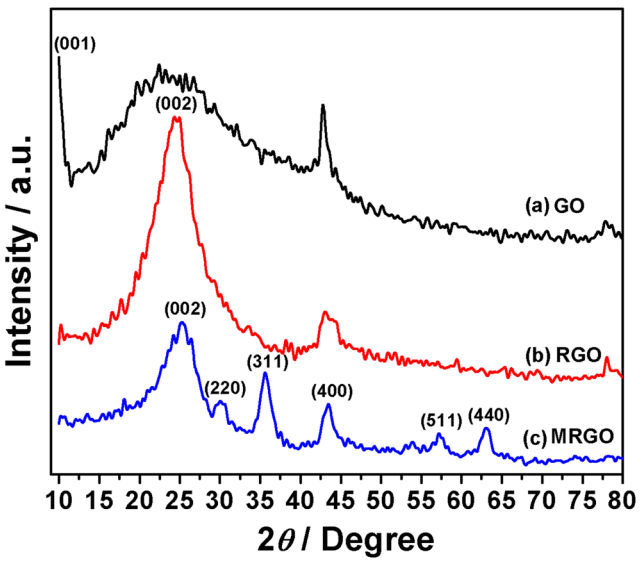

Fig. 1 XRD patterns of **a** GO, **b** RGO, and **c** MRGO

MRGO nanocomposite. The crystallite size of MNPs was estimated by the Debye Sherrer's formula using the most intense peak of Fe_3O_4, and it was found to be around 6.3 nm. When a permanent magnet was placed near the vial containing dispersed MRGO, it was attracted to the magnet, and within few seconds, the solution became clear (see Fig. S1 of the supporting information).

TEM micrographs of RGO and MRGO are shown in Fig. 2 a and b, respectively, along with corresponding selected area electron diffraction (SAED) pattern in the inset. Both images display the RGO sheets of few layers stacked over each other with nominal wrinkled basal planes [48]. For MRGO, decoration of MNPs on RGO sheets can be observed. The average size of MNPs anchored on the RGO sheet was found to be around 30 nm, and size distribution is shown in the supporting information (Fig. S2). Random size distribution was observed due to an agglomeration of nanoparticles. Both the images display RGO sheets of few layers stacked over each other with nominal wrinkled basal planes. Decoration of MNPs on the graphene sheets has not changed the morphology of RGO. Indexing of SAED patterns corroborates well with XRD results confirming the coexistence of RGO and Fe_3O_4 phases in MRGO.

The FTIR spectra of GO, RGO, and MRGO are shown in Fig. S3 of the supporting information. The spectrum of GO (Fig. S3(a)) displays the oxidation of graphite through the presence of oxygen-containing functional groups like C=O, C–OH, and C–O [49]. The peak around 1624 cm^{-1} is due to the C=C stretching of unoxidized domains of graphite. The broad absorption at 3422 cm^{-1} in all three spectra of Fig. S3 is due to the stretching of the O–H group of adsorbed water molecules. In the spectra of RGO and MRGO, the intensities of oxygen-containing functional groups are substantially reduced as compared with that for GO, indicating the successful reduction of GO by DMF. However, these peaks did not disappear entirely, suggesting the partial reduction of GO. An additional absorption peak at 435 cm^{-1} in MRGO spectra corresponding to Fe–O vibrations gives further evidence of the presence of magnetic oxides onto RGO [50].

The chemical states of the elements of GO, RGO, and MRGO were investigated by XPS. The survey spectra of GO, RGO, and MRGO are shown in Fig. 3a implying the presence of C 1s, O 1s, and Fe 2p (for MRGO) at 285, 530, and 711 eV, respectively [51]. Compared with GO, the declined O 1s peak and the enhanced C 1s peak indicate the existence of RGO [52]. Deconvolution spectra of C 1s and O 1s for RGO are shown in Fig. S4(a) and (b) of the supporting information, respectively. The deconvolution of the C 1s peak for MRGO (Fig. 3b) mainly displays nonoxygenated carbon C–C/C=C (284.7 eV) along with moderate contributions from C–O (286.4 eV) and O–C=O (289.3 eV) functional groups. This shows a good partial reduction of GO. In Fig. 3c, the O 1s spectrum deconvoluted into three peaks is presented. The three peaks at 530.2, 532.2, and 534.5 eV are attributed to oxygen in Fe_3O_4 lattice (Fe–O), a surface hydroxyl group (O–H), and lattice (C–O), respectively [53]. Figure 3 d shows the Fe 2p core-level XPS spectrum for MRGO. Peaks at 710.7 eV (Fe $2p_{3/2}$) and 724.1 eV (Fe $2p_{1/2}$) are assigned to Fe^{2+} state, and other two peaks at 712.5 eV (Fe $2p_{3/2}$) and 726.4 eV (Fe $2p_{1/2}$) are assigned to Fe^{3+} state in Fe_3O_4 [51]. Also, no peaks corresponding to Fe_2O_3 phases are observed, which confirms that MNPs decorated on RGO are pure magnetite.

Electrochemical behavior of RGO and MRGO in various electrolyte solutions

Different electrolyte solutions can show different electrochemical behavior for the same modified electrode depending on the chemical nature of electrolyte solutions. To establish various electrolyte solutions applicability in sensing and/or supercapacitive applications, the electrochemical performance of RGO and MRGO-modified electrodes were evaluated in various aqueous electrolyte solutions.

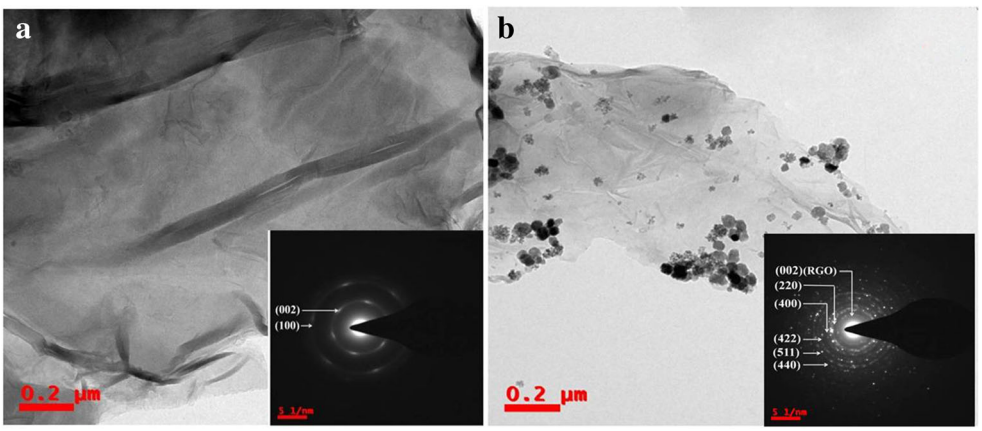

Fig. 2 TEM micrographs of **a** RGO and **b** MRGO (inset shows corresponding SAED pattern)

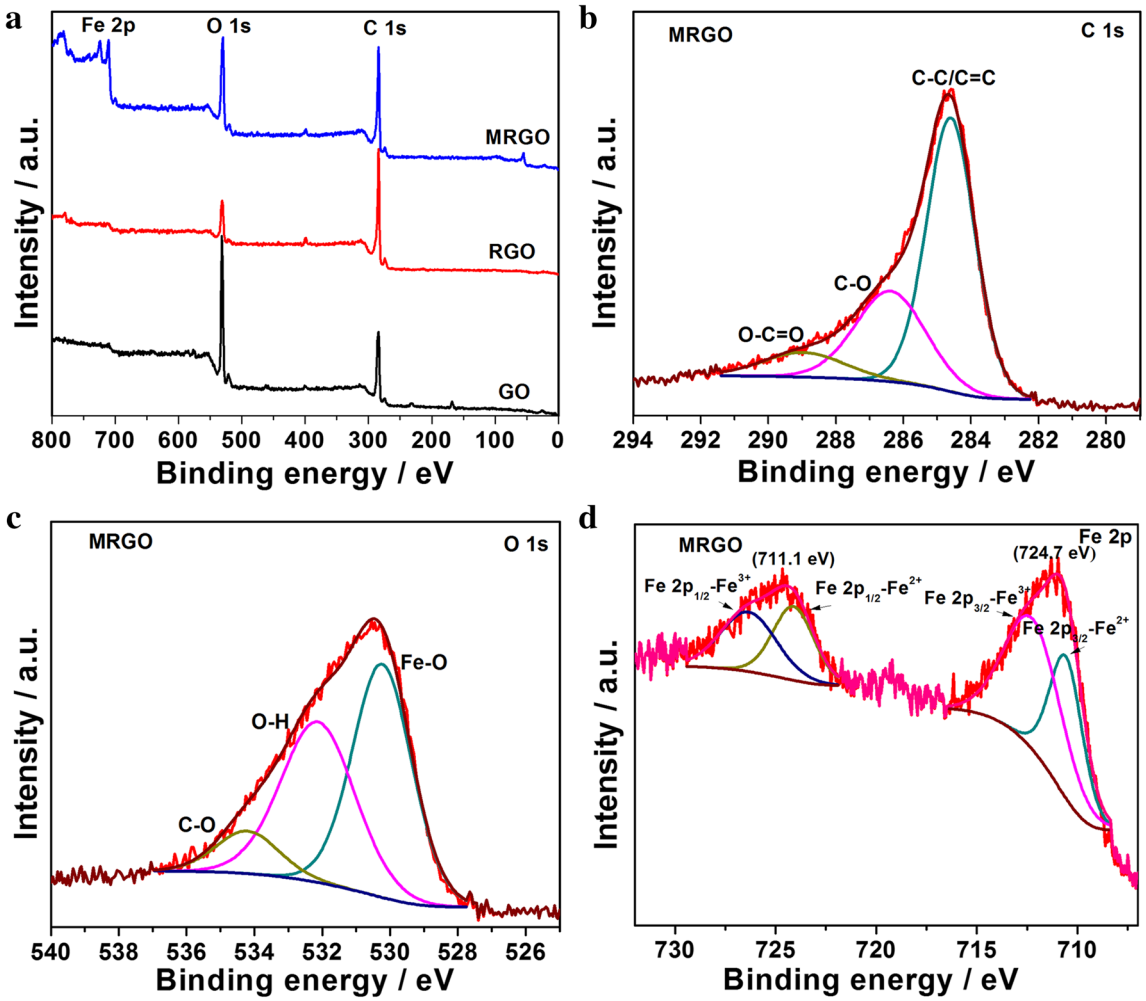

Fig. 3 **a** XPS survey spectra of GO, RGO, and MRGO. Deconvoluted XPS spectra of **b** C 1s, **c** O 1s, and **d** Fe 2p of MRGO

Electrochemical behavior of modified electrodes was investigated using CV in FC-PBS electrolyte solution in potential window − 0.1 to 0.7 V. The presence of 2 mM $K_3[Fe(CN)_6]$ in the 0.1 M PBS offers an extra complementary redox couple. This provides an electron buffer source for the reaction at the electrode–electrolyte solution interface [54]. Figure 4 a and b show the CV curves of RGO/GCE and MRGO/GCE electrodes, respectively, measured at scan rate of 10–100 mV s^{-1}. In Fig. 4 a, it can be seen that for RGO, the peak current has been negligibly increased with the scan rate. On the other hand, for MRGO (Fig. 4b), peak current has been significantly increased with the scan rate. This implies that the oxidation of $K_3[Fe(CN)_6]$ on the RGO/GCE electrode is very fast and is not limited by the scan rate. The current for MRGO

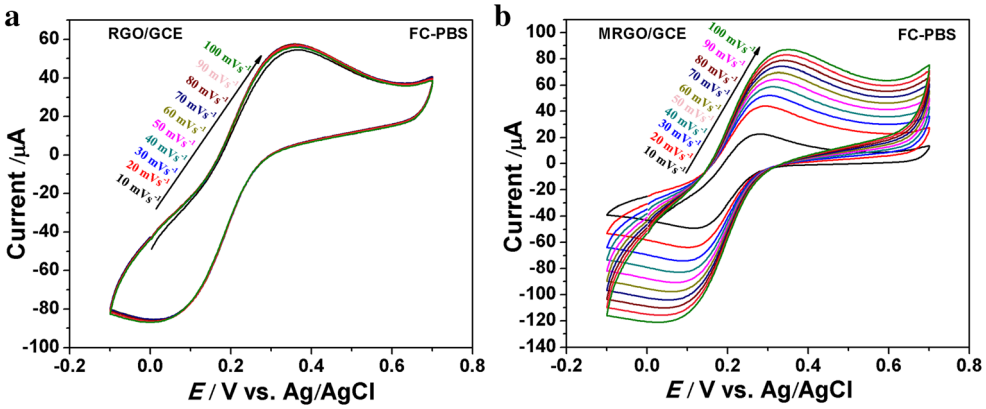

Fig. 4 CV curves of **a** RGO/GCE and **b** MRGO/GCE at scan rate of 10–100 mV s^{-1} for MRGO in FC-PBS electrolyte solution

increases rapidly at higher scan rate implying that redox reaction of $K_3[Fe(CN)_6]$ on the MRGO electrode is relatively slow and highly limited by the scan rate [55]. It can also be seen from Fig. 4 that, for both the RGO/GCE and MRGO/GCE electrodes, the scan rate affects the redox peak potentials. The oxidation peak potentials were shifted toward the positive direction, and the cathodic peak potentials were slightly shifted toward the negative direction with increasing scan rates. Shifting of peak potentials with scan rate may be attributed to the development of overpotential, which limits the faradic reaction [56, 57]. The magnitude of the anodic peak current (I_{pa}) for RGO/GCE is 57.29 μA, and it was increased to 64.33 μA for the MRGO/GCE measured at a scan rate of 50 mV s^{-1}. Using the anodic peak current values and surface area of the electrode, peak current density value for RGO/GCE and MRGO/GCE was found to be 1037.14 μA cm^{-2} and 1198.42 μA cm^{-2}. Liu et al. have obtained 861.9 μA cm^{-2} I_{pa} for Fe_3O_4/C/GCE in the electrolyte solution of 0.1 M PBS containing 0.5 mM $K_3[Fe(CN)_6]$ [58]. In a similar electrolyte solution, Caiet et al. have obtained 42.43 μA cm^{-2} I_{pa} for Fe_2O_3/GO/GCE [59]. Radhakrishnan et al. have obtained 350 μA cm^{-2} I_{pa} value for Fe_2O_3-RGO/GCE in 1 mM $Fe(CN)_6$ in 0.1 M KCl [60]. Peak potential separation for MRGO ($\Delta E_{MRGO/GCE}$ = 0.24 V) was lower than that for RGO ($\Delta E_{RGO/GCE}$ = 0.34 V). The observed lower ΔE for MRGO reveals that the MRGO facilitates faster electron transfer towards the electrode in bulk solution [54]. Higher values of redox peak currents and lower magnitude of ΔE for MRGO imply that MRGO/GCE in PBS containing 2 mM $K_3Fe(CN)_6$ is suitable for electrochemical sensing application [61]. To further evaluate the reaction mechanism of MRGO/GCE, the peak current (I_p) is plotted against the square root of the scan rate ($\upsilon^{1/2}$) (see Fig. S5(a) of the supporting information). The high linearity of the I_p vs. $\upsilon^{1/2}$ plot indicates that the electro-oxidation reaction is controlled by diffusion in the electrolyte solution. Fig. S5(b) shows the linear regression line for ln I_p and ln υ plot for MRGO, which can give the information of the ion transfer process. The slope near one is attributed to the adsorption-controlled electrode process, and slope near 0.5 indicates a diffusion-controlled process [62]. For MRGO/GCE in FC-PBS electrolyte solution, linear relationship between ln(I_p) and ln(υ) can be expressed by the following equations:

$$\ln I_{pa} = 2.52 + 0.42 \cdot \ln(\upsilon) \quad \left(R^2 = 0.999\right), \tag{1}$$

$$\ln I_{pc} = 2.93 + 0.40 \cdot \ln(\upsilon) \quad \left(R^2 = 0.998\right), \tag{2}$$

The slope of ln(I_p) vs. ln(υ) plots for MRGO/GCE in the FC-PBS electrolyte solution is close to 0.5, indicating that the redox process on the modified electrode is controlled by the diffusion. The electrochemical active surface area of the modified electrodes was determined by the Randles–Sevcik equation at a scan rate of 50 mV s^{-1} [61, 62].

$$I_{pa} = \left(2.69*10^5\right) n^{\frac{3}{2}} A c D^{\frac{1}{2}} \upsilon^{\frac{1}{2}} \tag{3}$$

Here, I_{pa} is anodic peak current (A), n is number of electrons in the reaction (1 for $K_3Fe(CN)_6$), A is the electrochemically effective surface area of the working electrode (cm^2), c is the concentration of the reactant (mol cm^{-3}), D is the diffusion coefficient for $K_3Fe(CN)_6$, and υ is the scan rate (V s^{-1}). Using the anodic peak current of bare GCE, D may be calculated where the diameter of the bare electrode is 3 mm. Then using the anodic peak currents, the electrochemical active surface area of RGO/GCE and MRGO/GCE was calculated. The active electrochemical surface area was found to be 0.066 cm^2 and 0.075 cm^2 for RGO/GCE and MRGO/GCE, respectively, in FC-PBS electrolyte solution.

KCl is an ionic conducting solution, with K^+ and Cl^- ions having molar conductivity 73.5 cm^2 Ω^{-1} and 76.4 cm^2 Ω^{-1}, respectively, which may be useful to increase the electrochemical performance. The value of the peak current (I_p) depends on the nature and concentration of the chloride cation [63]. In further experiments, 0.1 M KCl was used as supporting electrolyte solution in addition to PBS and $K_3Fe(CN)_6$. The electrochemical behavior of modified electrodes was investigated in the FC-PBS-KCl electrolyte solution in potential window − 0.1 to 0.7 V. Figure 5 a and b show the CV curves of RGO/GCE and MRGO/GCE electrodes, respectively, measured at scan rates 10–100 mV s^{-1}. For both the RGO/GCE and MRGO/GCE electrodes with the increasing scan rate, redox peak potential separation and peak current were increased. The magnitude of the anodic peak current (I_{pa}) for RGO/GCE is 72.60 μA, and it was increased to 83.89 μA for the MRGO/GCE at a scan rate of 50 mV s^{-1}. Peak potential separation for RGO and MRGO was found to be the same ($\Delta E_{RGO/GCE} \approx \Delta E_{MRGO/GCE} \approx 0.11$ V). To evaluate the reaction mechanism of MRGO/GCE, the peak current (I_p) is plotted against the square root of the scan rate ($\upsilon^{1/2}$) (see Fig. S6(a) in the supporting information). The high linearity of the I_p vs. $\upsilon^{1/2}$ plot indicates that the electro-oxidation reaction is controlled by diffusion in the electrolyte solution [62]. Figure S6(b) displays a linear relationship between ln(I_p) and ln(υ) expressed by equations,

$$\ln I_{pa} = 1.74 + 0.68 \cdot \ln(\upsilon) \quad \left(R^2 = 0.994\right), \tag{4}$$

$$\ln I_{pc} = \ 1.74 + 0.69 \cdot \ln(\upsilon) \quad \left(R^2 = 1.0\right), \tag{5}$$

The slope of ln(I_p) vs. ln(υ) plots for MRGO/GCE in FC-PBS-KCl electrolyte solutions are close to 0.5, indicating that the redox process on the modified electrode is controlled by the diffusion. The electrochemical surface area was calculated by the Randles–Sevcik equation given in Eq. 3, and it was

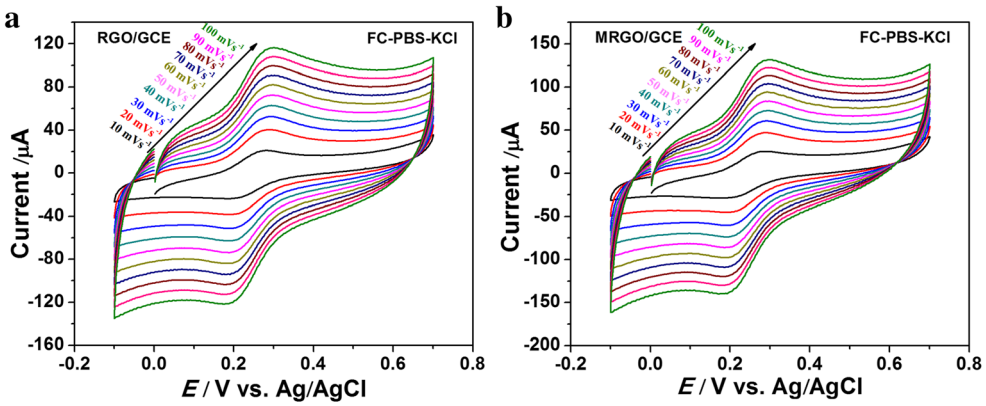

Fig. 5 CV curves of **a** RGO/GCE and **b** MRGO/GCE at scan rate of 10–100 mV s^{-1} for MRGO in FC-PBS-KCl electrolyte solution

found to be 0.085 cm^2 and 0.1 cm^2 for RGO/GCE and MRGO/GCE, respectively, in FC-PBS-KCl electrolyte solution. Zhiyong Xie et al. has obtained 0.148 cm^2 electrochemical active surface area for MRGO/SPCE [64].

In both the electrolyte solutions, with the increasing scan rate, peak current (I_p) was found to be increased for RGO and MRGO. This is due to the migration and diffusion of electrolyte ions into the electrode. For low scan rates, the growth of a thick diffusion layer on the electrode restricts the drift of electrolyte ions towards the electrode. This results in the lower current. At higher scan rates, diffusion layer does not grow much on the electrode surface. Hence at a high scan rate, electrolytic ions drift increases towards the electrode, which facilitates the increase in the current [56]. Compared with pure RGO/GCE, the higher peak current for MRGO/GCE in both the electrolyte solutions is due to the synergistic effect of magnetic nanoparticles and RGO arising from the high redox activity of MNPs and good conductivity of RGO which leads to the fast electron transfer [29, 54]. The different electrochemical performance of modified electrodes in different electrolyte solutions arises from different physical properties of the ions of electrolyte solutions [65]. These properties include the ionic radius, radius of ionic hydration sphere, molar conductivity, and ionic mobility. The well-defined quasi-reversible peaks could be observed at the RGO/GCE and MRGO/GCE CV curves. Anodic peak current of MRGO/GCE in the FC-PBS-KCl electrolyte solutions is greater than that in the FC-PBS electrolyte solution. Increased I_p may be due to increased electrical conductivity of the electrolyte solution owing to the presence of 0.1 M KCl as a supporting electrolyte solution to PBS and $K_3Fe(CN)_6$. Kiryushov et al. have observed an increase in the reduction peak current of a $K_3Fe(CN)_6$ solution on a deactivated graphite-epoxy electrode with the increasing concentration of KCl [63]. Morris et al. have also observed an increase in peak current as KCl concentration was increased in ferri and ferrocyanide solutions for graphite electrode [66]. It is well-known that some oxygen-containing functional groups, such as –OH, –COOH present on RGO, can lead to the sp^3-hybridized carbon atoms. The process of electrochemical reduction in 0.1 M KCl solution in the range of − 0.1 to 0.7 V may remove these oxygen functional groups and restore sp^2-hybridized carbon atoms [67]. Restoration of sp^2-hybridized carbon atoms results in superior electron transport property, which can accelerate the electron transfer at the interface of the MRGO electrode/electrolyte solutions. Also, $\Delta E_{MRGO/GCE}$ is lower in an electrolyte solution containing KCl (0.11 V) than that in an electrolyte solution without KCl (0.22 V). Pooja Devi et al. have reported 0.22 V $\Delta E_{MRGO/GCE}$ in 5 mM ferri/ferro solution in the presence of 0.1 M KCl [54]. Moreover, the electrochemical surface area of MRGO/GCE in FC-PBS-KCl electrolyte solution (0.2240 cm^2) was found to be higher than that in the FC-PBS electrolyte solution (0.09 cm^2). Higher peak current, lower peak potential separation, and higher electrochemical surface area of MRGO/GCE in the FC-PBS-KCl electrolyte solution show that this electrolyte solution is a suitable candidate for the electrochemical sensing application. Next, is discussed to study the electron transfer properties at the surface of the modified electrodes in both the FC-PBS and FC-PBS-KCl electrolyte solution, EIS investigations are carried out and are presented in the supporting information (Fig. S7).

Aqueous electrolyte solutions of Na_2SO_4 and KOH with Na^+, SO_4^{2-}, K^+, and OH^- ions having ionic mobility (μ) 5.2, 8.3, 7.6, 20.6 × 10^{-5} m^2 s^{-1} V^{-1}, respectively, can be useful for capacitive performance [68]. These electrolyte solutions have lower cost, environment-friendly, high operating stability, high ionic conductivity, and proton transport compared with organic electrolyte solutions [44]. Electrochemical performance of RGO/GCE and MRGO/GCE was investigated by CV, GCD, and EIS measurements in 1 M Na_2SO_4 and 1 M KOH electrolyte solutions. Figure 6 a and b show the CV curves of RGO/GCE and MRGO/GCE electrodes, respectively, at scan rates 10–100 mV s^{-1} in 1 M Na_2SO_4 within the potential range of − 0.1 to 0.7 V. Figure 6 c and d show the CV curves of RGO/GCE and MRGO/GCE electrodes, respectively, at scan rates 10–100 mV s^{-1} in 1 M KOH within the potential range of − 0.1 to 0.7 V. In both the electrolyte solutions, the CV curves of RGO/GCE and MRGO/GCE

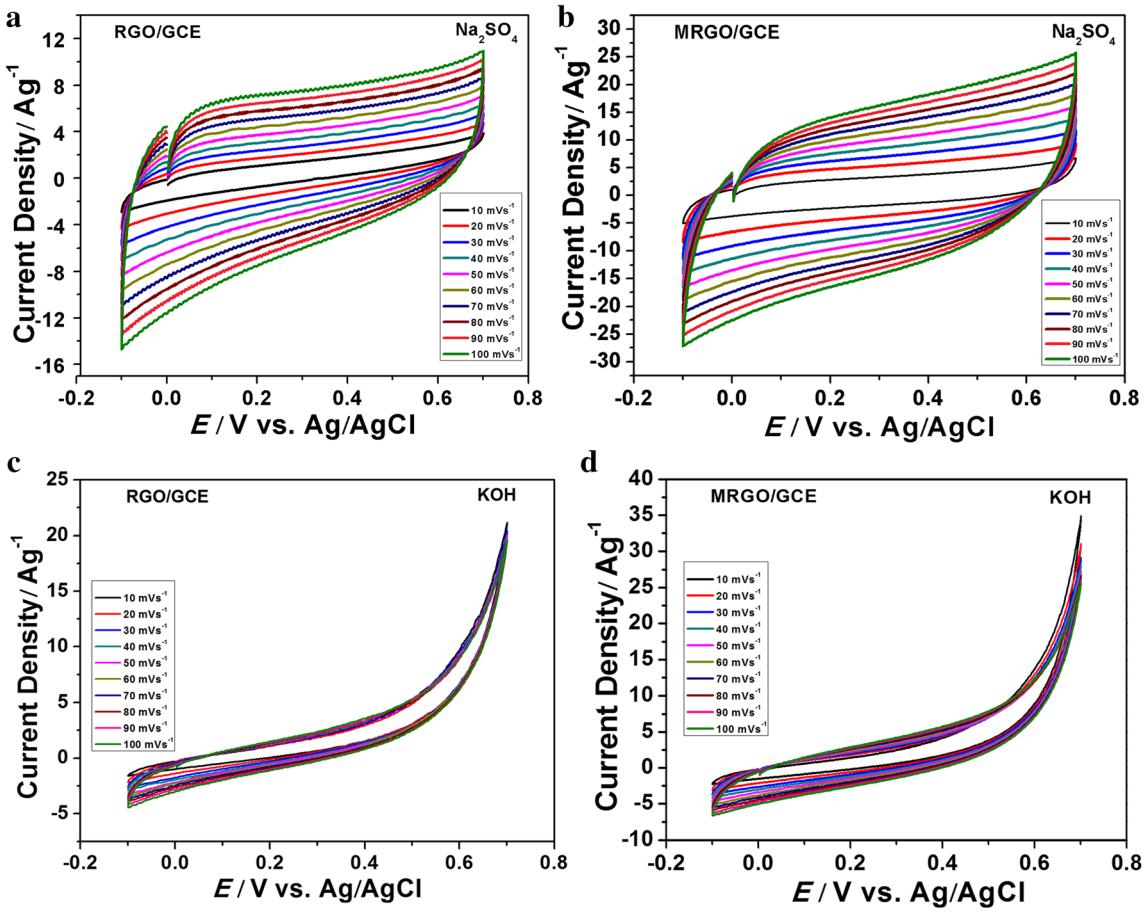

Fig. 6 CV curves of **a** RGO/GCE and **b** MRGO/GCE in 1 M Na_2SO_4 electrolyte solution and **c** RGO/GCE and **d** MRGO/GCE in 1 M KOH electrolyte solution at scan rate of 10–100 mV s^{-1}

electrodes show nearly rectangular shape, without redox peaks, which is typical behavior of capacitor. Kumar et al. have observed rectangular shape CV for RGO indicating EDLC behavior and CV curves of Fe_3O_4 with redox peaks indicating pseudocapacitance [53]. For MRGO nanocomposite-modified electrodes, the rectangular and symmetric CV curves are due to the combination of both the contributions, viz. significant contribution of EDLC from RGO and minor contribution of faradic pseudocapacitance corresponding to the reversible reaction of Fe^{2+} to Fe^{3+} in Fe_3O_4 MNPs [69]. The absence of redox peaks in MRGO CV may be attributed to the depression of the Fe_3O_4 pseudocapacitance feature due to the lower content of Fe_3O_4 in the composite [70]. The rectangular and symmetrical shape of CV curves does not change even at a higher scan rate which can be attributed to the lower resistance and excellent reversibility [53].

Capacitive behaviors of modified electrodes were studied using the GCD technique. The charge–discharge measurements of RGO/GCE and MRGO/GCE were carried out in 1 M Na_2SO_4 and 1 M KOH electrolyte solution between 0 and 0.7 V potential range (vs. Ag/AgCl) at various applied current densities (Fig. 7a–d). Modified electrodes show moderately symmetric and triangular charge–discharge curves in Na_2SO_4 and KOH electrolyte solutions without any noticeable *IR* drop, which shows good stability during the cyclic test. The slight curvature in charge–discharge curves indicates that the supercapacitive behavior is influenced by both electric double layer and pseudocapacitance [71]. The specific capacitance from GCD was calculated by the equation

$$C_{sp} = \frac{I\mathrm{d}t}{mdv} \tag{6}$$

where C_{sp} is specific capacitance (Fg^{-1}), I is the discharge current (A), dt is discharge time (s), m is the mass of the active material on the surface (g), and dv is the potential window during the discharge process. It is apparent that the discharge time for MRGO is longer than that of RGO for the same current density. Specific capacitance values for MRGO and RGO at various current densities are given in Table S1 of the supporting information. In both the Na_2SO_4 and KOH electrolyte solutions, capacitance of MRGO is higher than that of

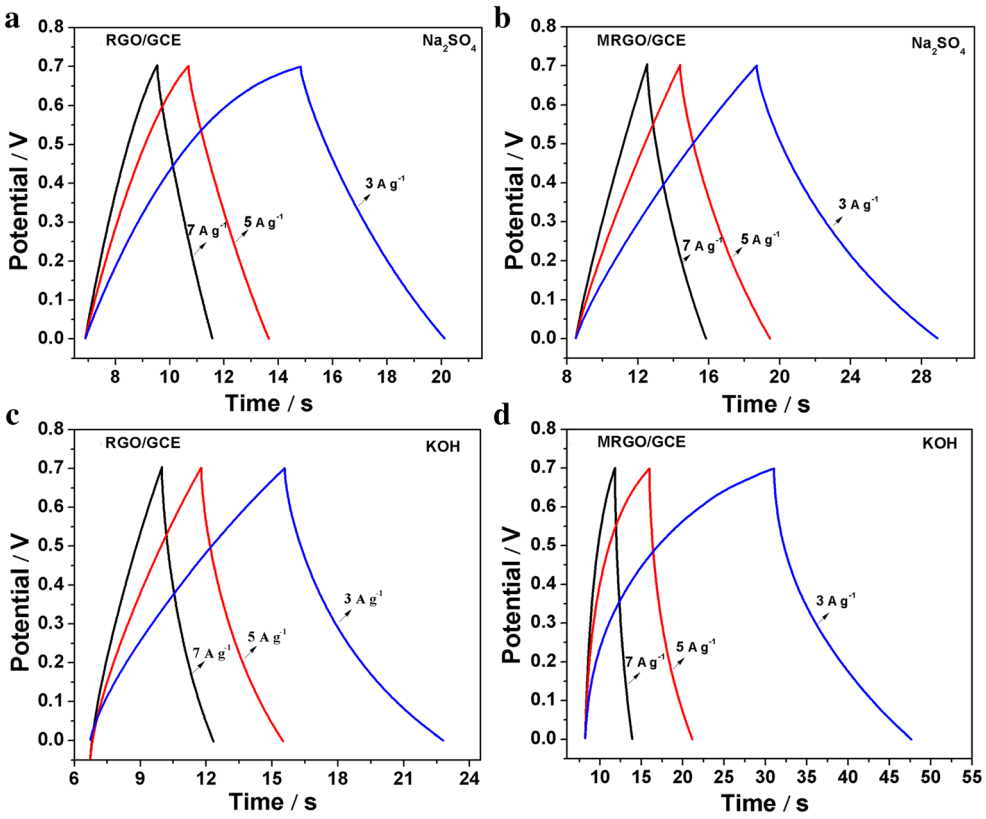

Fig. 7 GCD curves of **a** RGO/GCE and **b** MRGO/GCE in 1 M Na_2SO_4 and **c** RGO/GCE and **d** MRGO/GCE in 1 M KOH at different current densities

RGO. In this study, we focused on the electrochemical behavior of synthesized materials in different electrolyte solutions instead of improving its supercapacitive behavior. Comparison of the capacitance values with the relevant literature is presented in Table S2 of the supporting information.

At higher current density, the capacitance is reduced due to weaker interaction between the ions and electrode [9]. In both the electrolyte solutions, the specific capacitance of MRGO nanocomposite is higher than that of RGO. This can be ascribed to the synergetic effect of Fe_3O_4 nanoparticles and RGO. RGO provides a highly conductive path for electron transport during the redox processes. The incorporation of magnetic nanoparticles on RGO may avoid the restacking of RGO sheets which improves electronic and ionic pathways resulting in high double-layer capacitance [72]. In addition, pseudocapacitance of MNPs also contributes to the observed capacitance. The comparison of GCD curves of MRGO/GCE in Na_2SO_4 and KOH electrolyte solutions at 3 A g^{-1} discharge current density presented in the supporting information (Fig. S8(a)). The specific capacitance for MRGO nanocomposite in KOH (180 F g^{-1}) is greater than in the Na_2SO_4 (114 F g^{-1}) electrolyte solution at 3 A g^{-1} discharge current density. Higher C_{sp} in KOH electrolyte solution than that in Na_2SO_4 electrolyte solution can be attributed to the unique properties of KOH aqueous electrolyte solution such as crystal radius, ionic mobility, molar conductivity, and Gibbs free energy [68]. Moreover, in alkaline electrolyte solutions, Fe_3O_4 has good stability and also the residual functional groups of RGO become more active [72]. The specific capacitance depends on hydration radius and molar conductivity. The smaller hydrated ionic radius of K^+ ions (3.31 Å) than the Na^+ ions (3.58 Å) results in easier diffusion of K^+ ions into the inner pores of the modified electrode [43]. Higher molar conductivity of K^+ and OH^- ions in KOH than that of Na^+ and SO_4^{2-} ions in Na_2SO_4 is also responsible for larger specific capacitance in K^+ ion-based aqueous electrolyte solution than that in Na^+ ion-based aqueous electrolyte solution [65]. Cyclic stability is an important parameter for estimating the supercapacitive performance. To investigate the cyclic stability of MRGO, GCD measurements were repeated for 2000 consecutive cycles at 3 A g^{-1} in KOH and Na_2SO_4 electrolyte solutions (Fig. S8(b) of the supporting information). MRGO retain 64% and 87% specific capacitance after 2000 cycles in Na_2SO_4 and KOH, respectively. Good cyclic life of MRGO is due to the carbon matrix which buffers the possible volume change in the continuous charge–discharge process [73]. The long-term cycling stability strongly depends on the cationic species. Na^+ ions have a larger hydrated ionic radius (3.58 Å) than the K^+ ions (3.31 Å). Hence after 2000 cycles, the specific capacitance of MRGO in Na_2SO_4 is less stable compared with that in KOH

electrolyte solution, maybe due to the significant composition damage caused by the insertion/de-insertion of large ionic radius of Na^+ during the charging–discharging cycles [74]. To get more insight into the charge transfer mechanism of the supercapacitor at the electrode/electrolyte solution interface, the impedance measurements were carried out in Na_2SO_4 and KOH electrolyte solutions and are demonstrated in the supporting information (Fig. S9).

Conclusions

MRGO nanocomposite was successfully synthesized by the one-pot solvothermal method. Structural and microstructural investigations done by XRD and TEM showed the formation of RGO and anchoring of MNPs on RGO sheets. The intensities of bands corresponding to the different functional groups in FTIR spectra demonstrated the reduction of GO to RGO and the presence of magnetic oxide in MRGO spectra. XPS study confirmed the good partial reduction of GO and the presence of Fe^{2+} and Fe^{3+} states in the pure magnetite phase in MRGO. RGO and MRGO-modified electrodes were found to be useful for sensing applications in FC-PBS and FC-PBS-KCl electrolyte solutions. Redox peak current (I_p) and peak potential separation (ΔE) for RGO/GCE at 50 mV s^{-1} in FC-PBS was observed to be 57.29 μA and 0.35 V, respectively, and that in FC-PBS-KCl was 72.6 μA and 0.11 V, respectively. On the other hand, I_p and ΔE for MRGO/GCE at 50 mV s^{-1} scan rate in FC-PBS was 64.33 μA and 0.24 V, respectively, and that in FC-PBS-KCl was 83.89 μA and 0.11 V, respectively. These findings demonstrate that MRGO in FC-PBS-KCl electrolyte solution can be a good electron pathway between electrode and electrolyte solution, desirable for sensing applications. Specific capacitance and R_{ct} of RGO/GCE in KOH was found to be 82 F g^{-1} at 3 A g^{-1} and 9 Ω, respectively. Interestingly, MRGO/GCE in KOH showed good supercapacitive properties in terms of specific capacitance (180 F g^{-1} at 3 A g^{-1}), R_{ct} (6 Ω), and cycling performance (87% after 2000 cycles) compared with RGO/GCE. In conclusion, the FC-PBS-KCl electrolyte solution is suitable for electrochemical sensing application and KOH electrolyte solution is suitable for supercapacitor applications. The overall superior electrochemical performance of MRGO compared with RGO is attributed to the synergistic effect of RGO and MNPs.

Supplementary Information The online version contains supplementary material available at https://doi.org/10.1007/s10008-020-04866-x.

Funding The study was funded by the Science and Engineering Research Board, Department of Science and Technology (DST-SERB), Government of India (no. EMR/2017/001810) and Human Resources Development Program (no. 20194030202470) of the Korea Institute of Energy Technology Evaluation and Planning (KETEP) grant funded by the Korean Government Ministry of Trade, Industry and Energy.

References

1. Ma S, Nam K, Yoon W, Yang X (2008) Electrochemical properties of manganese oxide coated onto carbon nanotubes for energy-storage applications. J Power Sources 178(1):483–489
2. Arie AA, Song JO, Lee JK (2009) Structural and electrochemical properties of fullerene-coated silicon thin film as anode materials for lithium secondary batteries. Mater Chem Phys 113(1):249–254
3. Yan JA, Chou MY (2010) Oxidation functional groups on graphene: structural and electronic properties. Phys Rev B - Condens Matter Mater Phys 82(12)
4. Ali MA, Kamil Reza K, Srivastava S, Agrawal VV, John R, Malhotra BD (2014) Lipid-lipid interactions in aminated reduced graphene oxide interface for biosensing application. Langmuir 30(14):4192–4201
5. Dubey R, Guruviah V (2019) Review of carbon-based electrode materials for supercapacitor energy storage. Ionics (Kiel) 25(4):1419–1445
6. Adhikari BR, Govindhan M, Chen A (2015) Carbon nanomaterials based electrochemical sensors/biosensors for the sensitive detection of pharmaceutical and biological compounds. Sensors (Switzerland) 15(9):22490–22508
7. Borenstein A, Hanna O, Attias R, Luski S (2017) Carbon-based composite materials for supercapacitor electrodes : a review. J Mater Chem A Mater Energy Sustain 5(25):12653–12672
8. Krishnamoorthy K, Veerapandian M, Yun K, Kim SJ (2013) The chemical and structural analysis of graphene oxide with different degrees of oxidation. Carbon N Y 53:38–49
9. Madhuvilakku R, Alagar S, Mariappan R, Piraman S (2017) Green one-pot synthesis of flowers-like Fe_3O_4/rGO hybrid nanocomposites for effective electrochemical detection of riboflavin and low-cost supercapacitor applications. Sensors Actuators B Chem 253:879–892
10. Pei S, Cheng HM (2012) The reduction of graphene oxide. Carbon N Y 50(9):3210–3228
11. Pumera M (2010) Graphene-based nanomaterials and their electrochemistry. Chem Soc Rev 39(11):4146–4157
12. Bai H, Li C, Shi G (2011) Functional composite materials based on chemically converted graphene. Adv Mater:1089–1115
13. Schniepp HC, Li J, Mcallister MJ et al (2006) Functionalized single graphene sheets derived from splitting graphite oxide. J Phys Chem B 2:8535–8539
14. Schwenke AM, Hoeppener S, Schubert US (2015) Microwave synthesis of carbon nanofibers-the influence of MW irradiation power, time, and the amount of catalyst. J Mater Chem A 3(47):23778–23787
15. Dubin S, Gilje S, Wang K, et al (2010) A one-step, solvothermal reduction method for producing reduced graphene oxide dispersions in organic solvents. Am Chem Soc 4:3845–3852
16. Sinan N, Unur E (2016) Fe_3O_4/carbon nanocomposite: investigation of capacitive & magnetic properties for supercapacitor applications. Mater Chem Phys 183:571–579
17. Li L, Gao P, Gai S, He F, Chen Y, Zhang M, Yang P (2016) Ultra small and highly dispersed Fe_3O_4 nanoparticles anchored on reduced graphene for supercapacitor application. Electrochim Acta 190:566–573
18. Zhang X, Sun X, Chen Y, Zhang D, Ma Y (2012) One-step solvothermal synthesis of graphene / Mn_3O_4 nanocomposites and their electrochemical properties for supercapacitors. Mater Lett 68:336–339

19. Stankovich S, Dikin DA, Dommett GHB, Kohlhaas KM, Zimney EJ, Stach EA, Piner RD, Nguyen SBT, Ruoff RS (2006) Graphene-based composite materials. Nature 442(7100):282–286
20. Nguyen ST, Jung I, Dikin DA et al (2007) Graphene−silica composite thin films as transparent conductors. Nano Lett 7:1888–1892
21. Jadhav HS, Thorat GM, Kale BB, Seo JG (2017) Mesoporous Mn reduced graphene oxide (rGO) composite with enhanced electrochemical performance for Li-ion battery. Dalton Trans 46(30): 9777–9783
22. Juan Yang A, Yu C (2016) Electroactive Edge site-enriched nickel-cobalt sulfide into graphene Frameworks for high-performance asymmetric supercapacitors. R Soc Chem 9:1299–1307
23. Zhao Y, Song X, Song Q, Yin Z (2012) A facile route to the synthesis copper oxide/reduced graphene oxide nanocomposites and electrochemical detection of catechol organic pollutant. R Soc Chem:6710–6719
24. Sreeprasad TS, Maliyekkal SM, Lisha KP, Pradeep T (2011) Reduced graphene oxide-metal/metal oxide composites : facile synthesis and application in water purification. J Hazard Mater 186(1): 921–931
25. Chang MS, Kim T, Kang JH et al (2015) The effect of surface characteristics of reduced graphene oxide on the performance of a pseudocapacitor. 2D Mater 2:14007
26. Usman AA, Mashuri (2019) Magnetic properties of rGO/Fe_3O_4 microparticles composites based on natural materials. In: AIP Conference Proceedings
27. Mondal S, Rana U, Malik S (2017) Reduced graphene oxide/Fe_3O_4/polyaniline nanostructures as electrode materials for an all-solid-state hybrid supercapacitor. J Phys Chem C 121(14):7573–7583
28. Liang C, Zhai T, Wang W, Chen J, Zhao W, Lu X, Tong Y (2014) Fe_3O_4/reduced graphene oxide with enhanced electrochemical performance towards lithium storage. J Mater Chem A 2(20):7214–7220
29. Waifalkar PP, Chougale AD, Kollu P, Patil PS, Patil PB (2018) Magnetic nanoparticle decorated graphene based electrochemical nanobiosensor for H_2O_2 sensing using HRP. Colloids Surf B: Biointerfaces 167:425–431
30. Wasiński K, Walkowiak M, Półrolniczak P, Lota G (2015) Capacitance of Fe_3O_4/rGO nanocomposites in an aqueous hybrid electrochemical storage device. J Power Sources 293:42–50
31. Yu L, Wu H, Wu B (2014) Magnetic Fe_3O_4-reduced graphene oxide nano-composites-based electrochemical biosensing. Nano Lett 6(3):258–267
32. Hoan NTV, Thu NTA, Van Duc H et al (2016) Fe_3O_4/Reduced graphene oxide nanocomposite: synthesis and its application for toxic metal ion removal. J Chemother 2016
33. Qin Y, Long M, Tan B, Zhou B (2014) RhB adsorption performance of magnetic adsorbent Fe_3O_4/RGO Composite and its regeneration through a Fenton-like reaction. Nano-Micro Lett 6(2):125–135
34. Liu S, Zhou L, Yao L, Chai L, Li L, Zhang G, Kankan, Shi K (2014) One-pot reflux method synthesis of cobalt hydroxide nanoflake-reduced graphene oxide hybrid and their NOx gas sensors at room temperature. J Alloys Compd 612:126–133
35. Zhu S, Chen M, Ren W, Yang J, Qu S, Li Z, Diao G (2015) Microwave assisted synthesis of α-Fe_2O_3/reduced graphene oxide as anode material for high performance lithium ion batteries. New J Chem 39(10):7923–7931
36. Liu Y, Guan M, Feng L, Deng S (2013) Facile and straightforward synthesis of superparamagnetic reduced graphene oxide – Fe_3O_4 hybrid composite by a solvothermal reaction. Nanotechnology: 025604
37. Singh RK, Kumar R, Singh DP (2016) Graphene oxide: strategies for synthesis, reduction and frontier applications. RSC Adv 6(69): 64993–65011
38. Ullah W, Anwar AW, Majeed A et al (2015) Cost-effective and facile development of Fe_3O_4 –reduced graphene oxide electrodes for supercapacitors. Mater Technol 30:144–149
39. Li T, Qin A, Yang L, Chen J, Wang Q, Zhang D, Yang H (2017) In situ grown Fe_2O_3 single crystallites on reduced graphene oxide nanosheets as high performance conversion anode for sodium-ion batteries. ACS Appl Mater Interfaces 9(23):19900–19907
40. Yang S, Cao C, Li G, Sun Y, Huang P, Wei F, Song W (2015) Improving the electrochemical performance of Fe_3O_4 nanoparticles via a double protection strategy through carbon nanotube decoration and graphene networks. Nano Res 8(4):1339–1347
41. Peik-See T, Pandikumar A, Nay-Ming H, Hong-Ngee L, Sulaiman Y (2014) Simultaneous electrochemical detection of dopamine and ascorbic acid using an iron oxide/reduced graphene oxide modified glassy carbon electrode. Sensors (Switzerland) 14(8):15227–15243
42. Gao Y, Wu D, Wang T, Jia D, Xia W, Lv Y, Cao Y, Tan Y, Liu P (2016) One-step solvothermal synthesis of quasi-hexagonal Fe_2O_3 nanoplates/graphene composite as high performance electrode material for supercapacitor. Electrochim Acta 191:275–283
43. Qu QT, Wang B, Yang LC, Shi Y, Tian S, Wu YP (2008) Study on electrochemical performance of activated carbon in aqueous Li_2SO_4, Na_2SO_4 and K_2SO_4 electrolytes. Electrochem Commun 10(10):1652–1655
44. Barzegar F, Momodu DY, Fashedemi OO, Bello A, Dangbegnon JK, Manyala N (2015) Investigation of different aqueous electrolytes on the electrochemical performance of activated carbon-based supercapacitors. RSC Adv 5(130):107482–107487
45. Zhou D, Zhang TL, Han BH (2013) One-step solvothermal synthesis of an iron oxide-graphene magnetic hybrid material with high porosity. Microporous Mesoporous Mater 165:234–239
46. Habte AT, Ayele DW, Hu M (2019) Synthesis and characterization of reduced graphene oxide (rGO) started from graphene oxide (GO) using the tour method with different parameters. Adv Mater Sci Eng 2019:1–9
47. Online VA, Feng Z, Zhang C et al (2013) RSC Advances An easy and eco-friendly method to prepare reduced additive for $LiFePO_4$ cathode materials 3. R Soc Chem 3(4408–44):4408–4415
48. Shalaby A, Nihtianova D, Markov P et al (2015) Structural analysis of reduced graphene oxide by transmission electron microscopy. Bulg Chem Commun 47:291–295
49. Shen X, Wu J, Bai S, Zhou H (2010) One-pot solvothermal syntheses and magnetic properties of graphene-based magnetic nanocomposites. J Alloys Compd 506(1):136–140
50. Hardiansyah A, Rahimi Chaldun E, Fadyah Idzni A (2018) Magnetic reduced graphene oxide as advanced materials for adsorption of metal ions. J Sains Mater Indones 18(4):185
51. Li Y, Zhao C, Wen Y, Wang Y, Yang Y (2018) Adsorption performance and mechanism of magnetic reduced graphene oxide in glyphosate contaminated water. Environ Sci Pollut Res 25(21): 21036–21048
52. Yan F, Ding J, Liu Y, Wang Z, Cai Q, Zhang J (2015) Fabrication of magnetic irregular hexagonal-Fe_3O_4 sheets/reduced graphene oxide composite for supercapacitors. Synth Met 209:473–479
53. Kumar R, Singh RK, Vaz AR, Savu R, Moshkalev SA (2017) Self-assembled and one-step synthesis of interconnected 3D network of Fe_3O_4/reduced graphene oxide nanosheets hybrid for high-performance supercapacitor electrode. ACS Appl Mater Interfaces 9(10):8880–8890
54. Devi P, Sharma C, Kumar P, Kumar M, Bansod BKS, Nayak MK, Singla ML (2017) Selective electrochemical sensing for arsenite using rGO/Fe_3O_4 nanocomposites. J Hazard Mater 322(Pt A): 85–94
55. Sriprachuabwong C, Karuwan C, Wisitsorrat A, Phokharatkul D, Lomas T, Sritongkham P, Tuantranont A (2012) Inkjet-printed graphene-PEDOT:PSS modified screen printed carbon electrode for biochemical sensing. J Mater Chem 22(12):5478–5485

56. Chandel M, Moitra D, Makkar P, Sinha H, Hora HS, Ghosh NN (2018) Synthesis of multifunctional $CuFe_2O_4$ -reduced graphene oxide nanocomposite: an efficient magnetically separable catalyst as well as high performance supercapacitor and first-principles calculations of its electronic structures. RSC Adv 8(49):27725–27739
57. Alam M, Karmakar K, Pal M, Mandal K (2016) Electrochemical supercapacitor based on double perovskite Y_2NiMnO_6 nanowires. RSC Adv 6(115):114722–114726
58. Liu J, Dong S, He Q, Yang S, Xie M, Deng P, Xia Y, Li G (2019) Facile preparation of Fe_3O_4/C nanocomposite and its application for cost-effective and sensitive detection of tryptophan. Biomolecules 9(6)
59. Cai Z, Ye Y, Wan X et al (2019) Morphology–dependent electrochemical sensing properties of iron oxide–graphene oxide nanohybrids for dopamine and uric acid. Nanomaterials 9:1–19
60. Radhakrishnan S, Krishnamoorthy K, Sekar C et al (2014) Applied Catalysis B : Environmental A highly sensitive electrochemical sensor for nitrite detection based on Fe_2O_3 nanoparticles decorated reduced graphene oxide nanosheets. Appl Catal B Environ 148–149:22–28
61. Srivastava S, Kumar V, Ali MA, Solanki PR, Srivastava A, Sumana G, Saxena PS, Joshi AG, Malhotra BD (2013) Electrophoretically deposited reduced graphene oxide platform for food toxin detection. Nanoscale 5(7):3043–3051
62. Thu NTA, Van Duc H, Hai Phong N et al (2018) Electrochemical determination of paracetamol using Fe_3O_4/reduced graphene-oxide-based electrode. J Nanomater 2018
63. Kiryushov VN, Skvortsova LI, Aleksandrova TP (2011) Electrochemical behavior of the system ferricyanide-ferrocyanide at a graphite-epoxy composite electrode. J Anal Chem 66(5):510–514
64. Xie Z, Xu J, Xie F, Xiong S (2016) Electrochemical detection of as(III) by a rGO/Fe_3O_4 -modified screen-printed carbon electrode. Anal Sci 32(10):1053–1058
65. Zhang X, Wang X, Jiang L, Wu H, Wu C, Su J (2012) Effect of aqueous electrolytes on the electrochemical behaviors of supercapacitors based on hierarchically porous carbons. J Power Sources 216:290–296
66. Morris JB, Schempf JM (1959) Voltammetric studies at the graphite electrode in quiet solutions. Anal Chem 31(2):286–291
67. Liao W, Guo C, Sun L et al (2015) The electrochemical behavior of nafion/reduced graphene oxide modified carbon electrode surface and its application to ascorbic acid determination. Int J Electrochem Sci 10:5747–5755
68. Ghosh S, Mathews T, Gupta B, Das A, Gopala Krishna N, Kamruddin M (2017) Supercapacitive vertical graphene nanosheets in aqueous electrolytes. Nano-Struct Nano-Objects 10:42–50
69. Wang Z, Ma C, Wang H, Liu Z, Hao Z (2013) Facilely synthesized Fe_2O_3-graphene nanocomposite as novel electrode materials for supercapacitors with high performance. J Alloys Compd 552:486–491
70. Cheng JP, Shou QL, Wu JS, Liu F, Dravid VP, Zhang XB (2013) Influence of component content on the capacitance of magnetite/reduced graphene oxide composite. J Electroanal Chem 698:1–8
71. Ramachandran R, Saranya M, Velmurugan V, Raghupathy BPC, Jeong SK, Grace AN (2015) Effect of reducing agent on graphene synthesis and its influence on charge storage towards supercapacitor applications. Appl Energy 153:22–31
72. Wang D, Li Y, Wang Q, Wang T (2012) Nanostructured Fe_2O_3-graphene composite as a novel electrode material for supercapacitors. J Solid State Electrochem 16(6):2095–2102
73. Qi T, Jiang J, Chen H, Wan H, Miao L, Zhang L (2013) Synergistic effect of Fe_3O_4/reduced graphene oxide nanocomposites for supercapacitors with good cycling life. Electrochim Acta 114:674–680
74. Pal B, Yang S, Ramesh S, Thangadurai V, Jose R (2019) Electrolyte selection for supercapacitive devices: a critical review. Nanoscale Adv 1(10):3807–3835